Journal of
Materials Chemistry A

Journal of Materials Chemistry A Accepted Manuscript

PAPER

High-performance three-dimensional Ni-Fe layered double hydroxide/graphene electrode for water oxidation†

Xiaowen Yu, Miao Zhang, Wenjing Yuan, and Gaoquan Shi[*]

Water oxidation to evolve oxygen is the key step in water splitting and related to a variety of energy systems. Here, we report a facile electrodeposition process to immobilize nickel-iron layered double hydroxide (Ni-Fe LDH) nanoplates on three-dimensional electrochemically reduced graphene oxide (3D-ErGO) for water oxidation. This Ni-Fe LDH/3D-ErGO electrode has a three-dimensional interpenetrating network with nanosized Ni-Fe nanoplates uniformly decorated on graphene sheets. It has an electrochemical active surface area (EASA) 3.3 times that of conventional planar electrodes. The open porous structure of this electrode also makes its EASA fully accessible to electrolyte for water oxidation and easy releasing of oxygen gas. This electrode can be directly used for catalysing the oxygen evolution reaction (OER) in alkaline media without using binder and conductive additive, exhibiting a small overpotential of 0.259 V and a low Tafel slope of 39 mV dec^{-1}. It is outperforms that of precious IrO_2 catalyst in activity, kinetics, and electrochemical stability.

1. Introduction

Water splitting reaction consists of two half-reactions: hydrogen evolution reaction (HER) at cathode and oxygen evolution reaction (OER) at anode.[1] OER is the energy control step in the process of overall electrolysis of water, and it is closely related to various renewable energy systems (e.g., solar cells, metal-air batteries).[2] However, this half-reaction is frequently an obstacle to the whole water splitting process because of its high overpotential and sluggish kinetics.[3, 4] Thus, extensive efforts have been devoted to finding efficient catalysts for lowering the energy consumption and accelerating the kinetics of OER. Iridium (Ir) and ruthenium (Ru) oxides were tested to be active OER catalysts in both acidic and alkaline media.[1,5] Unfortunately, these rare metal oxides suffer from high costs and scarcity, as well as their poor long-term stability in alkaline media.[3,6] To address these issues, perovskites and first-row transition metal-based catalysts have been explored as replacements, because they are earth-abundant and relatively stable.[7–11] Among first-row transition metals, Fe^{3+} ions doped α-Ni(OH)$_2$ catalysts showed high OER activities, while the role of Fe^{3+} ions in increasing the OER activity is still unclear.[12] Several explanations were proposed, including that Fe^{3+} ions enhanced the electrical conductivity of NiOOH,[13] and the doping of α-Ni(OH)$_2$ with Fe^{3+} ions formed a Ni-Fe layered double hydroxide (Ni-Fe LDH) structure.[12–17]

On the other hand, the electrocatalytic activities of catalysts strongly depend on their structures and electrochemical active surface areas (EASAs).[18,19] Ni-Fe LDH has a layered structure and its interlayer space can be expanded by intercalating anions and water molecules between their neighboring slabs, providing OH$^-$ ions with enough space to access the active metal ions.[20,21] The catalytic activities of Ni-Fe LDH catalysts can also be enhanced by reducing their particle sizes to increase EASAs.[19,22] However, Ni-Fe LDH catalysts are insulators and easy to aggregate into large particles.[23] Therefore, carbon materials (e.g. carbon black, carbon nanotubes and graphene) have frequently been blended into Ni-Fe LDH catalysts to improve their conductivities and inhibit particle aggregation.[15, 20,24] Up to date, these Ni-Fe LDH/carbon hybrid catalysts were usually prepared by dip coating or solution casting on two-dimensional (2D) substrate electrodes to form compact films. Thus, their EASAs are small and most of the catalysts are inaccessible to electrolyte for OER. An electrode with three-dimensional (3D) porous structure can provide a large specific surface area for loading catalyst, and increasing the mass and electron transport kinetics; thus can notably improve the activity and efficiency of the catalyst.[1, 25–27] Here, we report an eco-friendly and facile electrochemical method to synthesis 3D graphene architecture with interpenetrating network for loading the nanoplates of Ni-Fe LDH. The resulting electrode can be directly used for OER. Its performance was tested to be

outperformed that of precious IrO_2 catalyst in terms of activity, kinetics and stability, exhibiting a low overpotential of 0.259 V and a small Tafel slope of 39 mV dec^{-1} in 1 M KOH.

2. Experimental Section

2.1 Preparation of the electrodes

Three-dimensional electrochemically reduced graphene oxide (3D-ErGO) electrode

Graphene oxide (GO) was synthesized from natural graphite powder by a modified Hummers method (ESI†).[28] 3D-ErGO electrode was fabricated by electrochemical reduction of GO sheets dispersed in an aqueous electrolyte. In order to remove bubbles produced at the surface of electrode in subsequent OER, we chose Au rotating disk electrode (Au-RDE, 5 mm diameter) as the working electrode. Prior to use, Au-RDE was polished with 0.5 and 0.05 μm alumina powder slurries successively, then washed by sonication with water and ethanol for three times, respectively. A platinum (Pt) foil was applied as the counter electrode and the potentials were referred to a saturated calomel electrode (SCE). An aqueous dispersion of GO (1.6 mg mL^{-1}) containing 0.1 M $LiClO_4$ (99%, Sinopharm Chemical Reagents Co. Ltd, Beijing, China) was used as the electrolyte. The electrochemical reduction process was carried out at a constant potential of −1.0 V for 10 s at room temperature by using a CHI 760D potentiostat-galvanostat (CH Instruments Inc.). The as-prepared electrode was washed with water and then immersed in water to remove the absorbed GO sheets and residual $LiClO_4$ salt. Finally, the electrode was kept in water to maintain its 3D architecture before use and it was nominated as 3D-ErGO electrode. For comparison, the as-obtained 3D-ErGO electrode was dried in air to collapse its porous structure into a compact film caused by capillary force, and the resulting electrode was nominated as 2D-ErGO electrode.

Ni-Fe LDH nanoplates/3D-ErGO electrode

Ni-Fe LDH nanoplates were electrochemically deposited onto the surface of a 3D-ErGO electrode from an mixed aqueous solution of 50 mM $Ni(NO_3)_2 \cdot 6H_2O$ and $Fe(NO_3)_3 \cdot 9H_2O$ with molar ratio of 4:1. The as-prepared 3D-ErGO electrode was used as the working electrode; the counter electrode and the reference electrode were the same to those described above. Typical potentiostatic deposition of Ni-Fe LDH nanoplates was carried out at −1.2 V for 10 s using a CHI 760D potentiostat-galvanostat. We also changed the deposition potential in the range of −0.8 to −1.3 V for studying its effects on the growth of Ni-Fe LDH nanoplates, and changed the molar ratios of Ni and Fe precursors to study the influences of Fe^{3+} doping in $Ni(OH)_2$ on OER. Successively, the prepared Ni-Fe/3D-ErGO electrodes were immersed in water to maintain their 3D morphology before use. Similarly, Ni-Fe/2D-ErGO electrodes were also prepared by using 2D-ErGO electrodes as the working electrodes for depositing Ni-Fe LDH nanoplates.

2.2 Characterizations

Scanning electron micrographs (SEM) were recorded on a field-emission Sirion-200 SEM (JEOL, Japan) at 10 kV. High-resolution transmission electron micrographs (HRTEM), scanning transmission electron micrographs (STEM), and energy dispersive spectra (EDS) were taken out by using a Tecnai F20 TEM operated at 200 keV. X-ray diffraction (XRD) was carried out on a D8 Advanced X-ray diffractometer with Cu Kα radiation (λ = 0.15418 nm, Bruker, Germany). Raman spectra were performed on a Renishaw Raman microscope with a 514-nm laser and 10% ND filler. X-ray photoelectron spectra (XPS) were obtained by using an ESCALAB 250 photoelectron spectrometer (Thermofisher, scientific, USA) with Al Kα (1486.6 eV) as the X-ray source (150 W), and a pass energy of 30 eV for a high resolution scan.

Samples for TEM measurements were prepared by dispersing the catalysts in ethanol and finally drop drying their diluted dispersions on copper grids. Samples for SEM, Raman, XPS studies were prepared by electrodepositing the catalysts on Au foils (100 μm thick) and then freeze dried. Samples for XRD examinations were prepared by collecting and drying the catalysts from Au foil. Before use, Au foil was cleaned by Piranha solution [H_2O_2 (30%) : H_2SO_4 (98%), 1:3, volume ratio; Caution: Piranha solution is a strong oxidizing regent that should be handled carefully] and then ultrasonicated with water until the pH of cleaning solution to be neutral.

2.3 Electrochemical studies

The EASAs of electrodes were measured in the aqueous solution of 5 mM $K_4Fe(CN)_6$ containing 1 M KCl by cyclic voltammetry (CV) and differential pulse voltammetry (DPV). CV studies were performed at a scan rate of 50 mV s^{-1} from 0 to 0.5 V (vs. SCE). For DPV studies, the potential range was also from 0 to 0.5 V with a pulse width and a period of 0.2 s and 0.5 s, respectively. The integrated area of the DPV wave is proportional to the EASA of electrode.

OER tests were performed in an O_2-purged aqueous solution of 1 M KOH (pH = 14). We chose Hg/HgO as the reference electrode, because the conventional silver/silver chloride electrode (Ag/AgCl) and SCE are unstable in alkaline media and they also release Cl^- ions with negative effects on OER.[22] Another pristine Hg/HgO electrode was used as a standard electrode for correcting the potentials and it was marked as Hg/HgO*. Before OER tests, it was acceptable when the open circuit voltage between these two reference electrodes was measured to be less than 5 mV. The potentials referred to Hg/HgO electrode for OER were all converted to reversible hydrogen electrode (RHE). The relationship between the potential referred to Hg/HgO ($E_{Hg/HgO}$) and that referred to RHE (E_{RHE}) is: $E_{RHE} = E_{Hg/HgO} + 0.098 + 0.059 \times pH$. All potentials reported here were corrected with 85% iR-compensation,[16] where i is the measured current, and R is the compensated resistance between the working and the reference electrodes. In our system, R was measured to be about 8 Ω for Ni-Fe/3D-ErGO electrode. The current densities were normalized to geometric surface area (0.196 cm^2) and the overpotential (η) was calculated using the equation: η = E_{RHE} -1.23. The catalyst
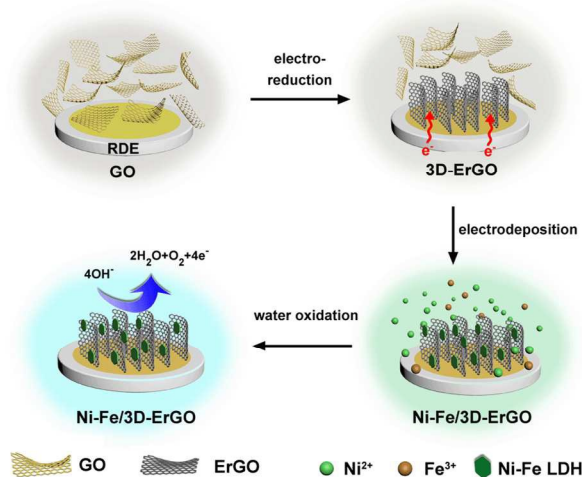
Scheme 1 Fabrication and application of Ni-Fe/3D-ErGO electrode.

modified Au-RDE was directly used as the working electrode, and a Pt foil was served as the counter electrode. All CV and Linear sweep voltammetry (LSV) curves were recorded at a slow sweep rate of 10 mV s^{-1} to weaken the capacitive current and the Tafel plots were performed at a much slower sweep rate of 1 mV s^{-1} to approach the steady state.

In the case of comparing the Ni-Fe/3D-ErGO with IrO$_2$ catalyst, the loading of the Ni-Fe/3D-ErGO catalyst on Au-RDE was controlled to be 0.14 mg cm^{-2}. This catalyst loading includes the weight of ErGO and it was measured by weighting. For the preparation of IrO$_2$ catalyst, 4 mg IrO$_2$ (powder from Alfa Asear without further purification) was dispersed in 768 μL of water, 200 μL of isopropanol and 32 μL 5 wt% Nafion solution by sonication. Then 7 μL of the catalyst ink was drop casted onto the Au-RDE, leading to a catalyst loading of 0.14 mg cm^{-2}. Finally, the as-prepared catalyst film was dried at room temperature.

A rotating ring disk electrode (RRDE) was used to measure the OER Faradaic efficiency of the typical Ni-Fe/3D-ErGO catalyst in 1 M KOH under N$_2$ atmosphere. The surface area of disk electrode is 0.25 cm^2. For the measurement of Faradaic efficiency of Ni-Fe/3D-ErGO catalyst at the current density of 1, 2, 5, or 10 mA cm^{-2}, a potential of 1.459, 1.469, 1.484, or 1.499 V was applied to the disk electrode, and a constant potential of 0.32 V (vs. RHE) was applied to the ring electrode. The collection efficiency (N) of the Ni-Fe/3D-ErGO catalyst was also determined by using RRDE in an aqueous solution of 0.1 M KOH and 10 mM K$_3$Fe(CN)$_6$ by LSV. The ring potential was controlled to be 0.55 V (vs. SCE), and the potential of disk electrode was swept from –0.6 to 0.4 V (vs. SCE) at a scan rate of 20 mV s^{-1} and a rotating rate of 100, 400, 900, 1600, or 2500 rpm. In both cases, the Ni-Fe/3D-ErGO catalyst was deposited on the disk electrode, and its growth condition is the same to that of depositing the catalyst on Au-RDE.
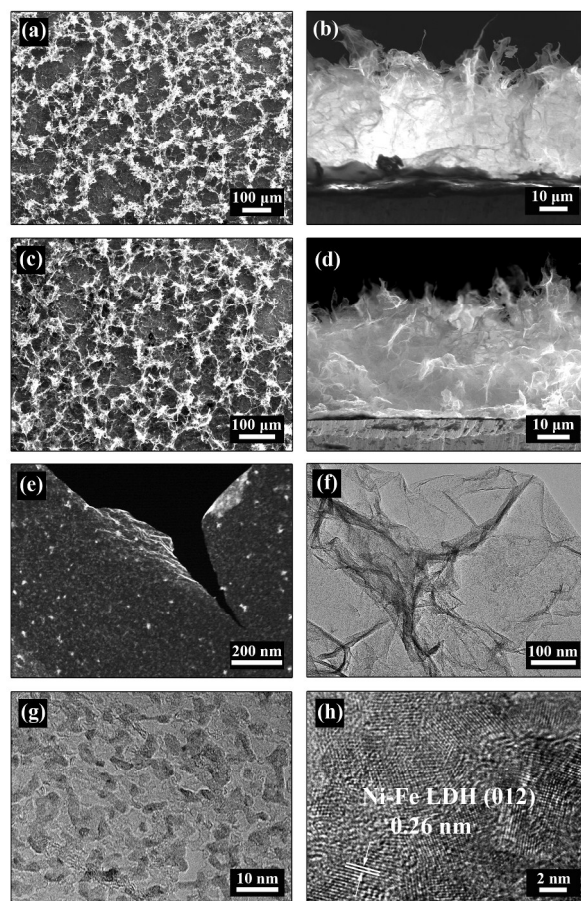
Fig. 1 (a) Top-view and (b) cross-sectional SEM images of 3D-ErGO on Au foil. (c) Top-view and (d) cross-sectional SEM images of Ni-Fe/3D-ErGO on Au foil. (e) STEM, (f, g) TEM and (h) HRTEM images of Ni-Fe/3D-ErGO.

3. Results and discussion

3.1 Morphology of the electrodes

The Ni-Fe/3D-ErGO electrode was fabricated via a two-step electrodeposition process as illustrated in Scheme 1. First, GO sheets in an aqueous dispersion (1.6 mg mL^{-1}) were electrochemically reduced at −1.0 V (vs. SCE) for 10 s to remove part of their oxygenated groups. During this process, the current density of electrolysis decreased gradually because of the thickening of ErGO layers (Fig. SO†).[29-31] Upon the driving of electric field and hydrophobic interaction, ErGO sheets were self-assembled on the surface of Au substrate electrode to form a porous 3D interpenetrating network (Fig. 1a, S2b†) with a thickness of about 30 μm (Fig. 1b). The pore sizes of the network were in the range of a few micrometers to tens of micrometers (Fig. 1a). The pore walls consist of thin layers of stacked graphene sheets (Fig. S2a†),[32] and they were nearly vertical to the surface of electrode (Fig. 1b), forming an open porous structure. The less number-density of ErGO sheets at the top part of 3D-ErGO layer revealed the self-confined and gradient growth of ErGO during the electroreduction process (Fig 1b). Thus, this architecture has a large accessible surface

area for mediating the nucleation and growth of foreign materials (e.g. Ni-Fe LDH particles).[27,33] Successively, the as-prepared 3D-ErGO was used as the working electrode for the electrodeposition of Ni-Fe LDH nanoplates. The deposition current density increased in first 1 s because of the further reduction of 3D-ErGO, and then decreased gradually caused by the depositing of insulating Ni-Fe LDH nanoplates (Fig. S3†). After loading of the Ni-Fe LDH nanoplates, the interpenetrating network of 3D-ErGO was mostly remained, while the thickness of the pore walls were slightly increased upon the coating of Ni-Fe LDH nanoplates (Fig. 1c, 1d and Fig. S4†). The Ni-Fe LDH nanoplates were uniformly decorated on the surfaces of ErGO sheets (Fig. 1e). This observation has also been confirmed by energy dispersive spectrometer (EDS) analysis (Fig. S5†), elemental mappings of carbon (C), oxygen (O), iron (Fe) and nickel (Ni) atoms (Fig. S6†), and the transmission electron microscope (TEM) characterizations (Fig. 1f and Fig. S7a†). The sizes of Ni-Fe LDH nanoplates were measured to be about 6~8 nm in length and 2~3 nm in width (Fig. 1g and Fig. S7b†). The HRTEM image demonstrates a fringe spacing of 0.26 nm, and this value agrees well with the spacing of (012) lattice plane of Ni-Fe LDH (Fig. 1h). The selected-area electron diffraction (SAED) pattern of Ni-Fe LDH nanoplates showed diffraction rings (inset of Fig. S7a†), indicating the polycrystalline nature of Ni-Fe LDH nanoplates. The labeled two diffraction rings correspond to the (012) and (003) lattice planes of Ni-Fe LDH with d-spaces of 0.26 and 0.15 nm, the other two diffraction rings were assigned to the two laps of diffraction spots of ErGO (inset of Fig. S2b†). The EDS mapping recorded from the cross-section of Ni-Fe/3D-ErGO electrode indicated that Ni-Fe LDH nanoplates were not only loaded on the surface of 3D-ErGO, but also embedded into the interpenetrating network (Fig. S8†).

3.2 Structure

The X-ray diffraction (XRD) pattern (Fig. 2a) of GO gives a (001) diffraction peak at $2\theta = 11^\circ$, corresponding to a d-space of 0.8 nm. This d-space is much larger than that of graphite (0.34 nm) because of the oxygenated functional groups in GO.[34] After the electroreduction of GO into ErGO, the (001) peak disappeared and a new broad diffraction peak at $2\theta = 24^\circ$ appeared. This peak is associated with the (002) graphic plane of ErGO sheets with a d-space of 0.37 nm, and its broad feature indicates the distortion from ordered arrangement of graphene sheets along their stacking direction. The smaller d-space of ErGO than that of GO suggests the existence of π-π stacking among ErGO sheets and the partial removal of oxygenated groups.[32] Upon loading of Ni-Fe LDH nanoplates on 3D-ErGO, three new weak peaks at $2\theta = 11.7^\circ$, 33.6°, 60.0° were observed, and they are assigned to the (003), (012), and (110) lattice planes of α-Ni(OH)$_2$ (JCPDS 38-0715), respectively. The weak intensities of these diffraction peaks were caused by the tiny sizes and the relatively low mass loading of Ni-Fe LDH nanoplates. The existence of the carbon material (3D-ErGO) resulted in a strong background noise that further reduced the apparent intensities of the XRD peaks related to Ni-Fe LDH
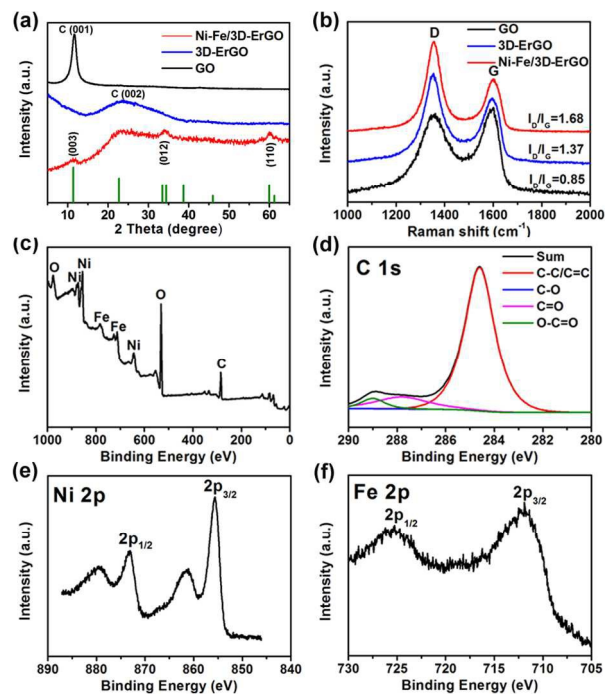
Fig. 2 (a) XRD patterns and (b) Raman spectra of GO, 3D-ErGO, Ni-Fe/3D-ErGO. (c) XPS survey spectrum, high-resolution (d) C 1s, (e) Ni 2p, and (f) Fe 2p spectra of Ni-Fe/3D-ErGO on Au foil.

nanoplates. The slight increase of the diffraction angle relative to (003) plane suggests a decrease in the d-spacing along the c-axis caused by the intercalation of anions in Ni(OH)$_2$ lattice.[35] The asymmetric nature of the reflection at about $2\theta = 33.6^\circ$ indicates the formation of turbostratic α-Ni(OH)$_2$ lattice.[36] This structure has a larger inter-sheet spacing than that of ordered β-Ni(OH)$_2$ lattice, and it is caused by the intercalation of anions and water molecules between the hydroxide sheets to neutralize the extra positive charges of Fe^{3+} relative to Ni^{2+} ions.[15] Furthermore, the peak related to the (002) plane of graphitic carbon was also shown with a slight decrease in its diffraction angle, further confirming that Ni-Fe LDH nanoplates embedded into the inner frame of ErGO sheets duo to the open porous structure of 3D-ErGO.

Raman spectroscopy was applied to characterize the structures of GO, 3D-ErGO and Ni-Fe/3D-ErGO (Fig. 2b). The spectrum of each sample has two prominent bands in the range of 1000 to 2000 cm^{-1}. The band at 1350 cm^{-1} is the D-band of carbon attributed to the structural defects or partially disordered graphitic domains. The band at around 1600 cm^{-1} is the G-band of carbon associated with graphitic domains.[37] The intensity ratio of D- and G-bands (I_D/I_G) can be used to evaluate the average sizes of crystalline sp^2 domains.[38] The I_D/I_G values of GO and ErGO were calculated to be 0.85 and 1.37, respectively, indicating the oxidized areas of GO sheets were partly restored upon reduction to form smaller conjugated domains in ErGO. The I_D/I_G value of Ni-Fe/3D-ErGO (1.68) is higher than that of ErGO, implying the further reduction of ErGO during the process of electrodeposition of Ni-Fe LDH nanoplates.

The survey scan of X-ray photoelectron spectroscopy (XPS) confirmed the existence of both Ni and Fe elements in the as-synthesized Ni-Fe/3D-ErGO hybrid catalyst (Fig. 2c). The atomic ratio of C, O, Ni, and Fe was measured to be 1.00: 1.24: 0.29: 0.07. The atomic ratio of Ni and Fe is about 4:1, and this value is identical to that of their nitrate precursors. The C 1s high-resolution survey spectrum (Fig. 2d) of Ni-Fe/3D-ErGO shows four types of carbons: C=C/C-C (284.6 eV); C-O (286.6 eV), C=O (287.8 eV) and O-C=O (289 eV).[21] The content of oxygenated groups of Ni-Fe/3D-ErGO, especially the C-O groups, is much lower than that of GO (Fig. S9a† and Fig. S9b†) or ErGO (Fig. S9c† and Fig. S9d†). These results further confirm that the functional groups of GO were partly removed upon electrochemical reduction and the GO sheets further reduced during the process of electrodeposition of Ni-Fe LDH nanoplates. The Ni 2p spectrum shows either a $Ni(OH)_2$ or NiOOH phase[16], which has a Ni $2p_{3/2}$ binding energy close to 855.6 eV (Fig. 2e). The high-resolution Fe 2p spectrum reflects that Fe species are mostly in their oxidation state of Fe^{3+} (Fig. 2f). The O 1s spectrum (Fig. S10†) shows a single peak of –OH groups at 531.0 eV, further confirming that Ni and Fe are in the phases of $Ni(OH)_2$ and $Fe(OH)_3$, respectively.[16]

3.3 The performances of the catalysts for OER

The electrocatalytic OER activities of Ni-Fe/3D-ErGO electrode were tested in alkaline media (1 M KOH). The as-prepared Ni-Fe/3D-ErGO modified Au-RDE (loading of catalyst = 0.14 mg cm^{-2}) was directly used as the working electrode in a standard three-electrode system under a rotating rate of 1600 rpm to get rid of the generated oxygen bubbles. The LSV polarization curves (Fig. 3a) were taken at a slow scan rate of 10 mV s^{-1} to minimize the capacitive current.[15] For comparison, Au, 3D-ErGO, Ni-Fe/Au, and Ni-Fe/2D-ErGO electrodes were also tested. The LSV curves of Au and 3D-ErGO electrodes show weak current densities within the tested potential range, indicating that they have negligible catalytic activities toward OER. In comparison, the curve of Ni-Fe/3D-ErGO exhibits a strong anodic current wall, and the potential applied to reach a current density of 10 mA cm^{-2} was measured to be 1.489 V (vs. RHE, corrected with iR-compensation). This value is about 0.019 and 0.072 V lower than those at Ni-Fe/2D-ErGO (1.508 V) and Ni-Fe/Au (1.561 V) electrodes (Fig. 3a). It should be noted here that Ni-Fe/2D-ErGO electrode performs better than Ni-Fe/Au electrode. This fact reflects that ErGO is a better substrate than Au for the growth of nanoparticles and the electron transfer during OER process. The wave centred at 1.430 V (vs. RHE) is related to the oxidation reaction of Ni^{2+} to Ni^{3+}.[13] The peak current of this wave at Ni-Fe/3D-ErGO electrode is much stronger than those at the other two Ni-Fe LDH electrodes because of the larger EASA of 3D-ErGO substrate. $[Fe(CN)_6]^{3-/4-}$ redox couples are well studied and widely used for comparing the EASAs of various carbon-based electrodes.[39] Fig. S11 (ESI†) illustrates the CV and DPV curves of 5 mM $K_4[Fe(CN)_6]$ containing 1 M KCl at different electrodes. The CV of 3D-ErGO electrode exhibits a pair of well-defined redox wave with a peak-to-peak potential
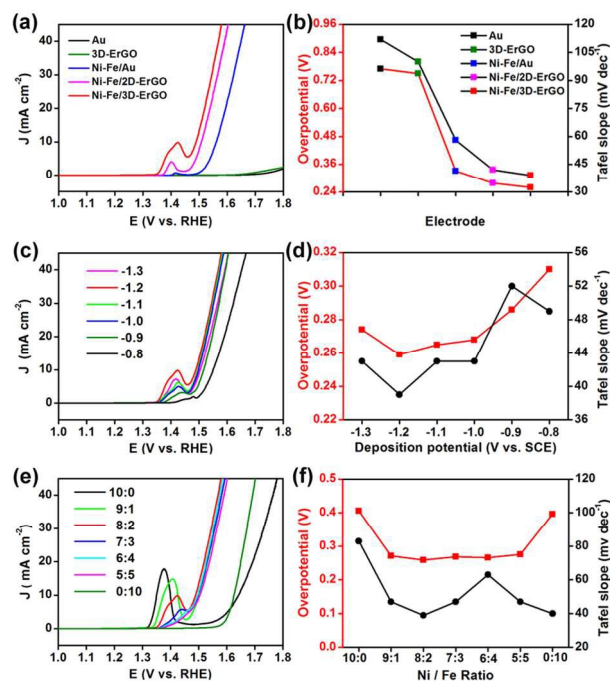
Fig. 3 (a) LSV curves of Au, 3D-ErGO, Ni-Fe/Au, Ni-Fe/2D-ErGO, and Ni-Fe/3D-ErGO electrodes. (b) Overpotential (at 10 mA cm^{-2}) and Tafel slope plots of Au, 3D-ErGO, Ni-Fe/Au, Ni-Fe/2D-ErGO, and Ni-Fe/3D-ErGO electrodes. (c) LSV curves of Ni-Fe/3D-ErGO electrodes prepared at the Ni-Fe deposition potentials ranging from −0.8 to −1.3 V. (d) Overpotential (at 10 mA cm^{-2}) and Tafel slope plots of Ni-Fe/3D-ErGO electrodes prepared at different Ni-Fe LDH deposition potentials. (e) LSV curves of the Ni-Fe/3D-ErGO electrodes prepared from the mixed nitrate precursors with different Ni/Fe ratios. (f) Overpotential (at 10 mA cm^{-2}) and Tafel slope plots of Ni-Fe/3D-ErGO electrodes prepared from the mixed nitrate precursors with different Ni/Fe ratios. LSV curves were recorded at a scan rate of 10 mV s^{-1}; electrolyte = 1 M KOH.

separation (ΔE_p) of 39 mV. The CV of 2D-ErGO electrode is similar to that of 3D-ErGO, while it has a larger ΔE_p of 84 mV because of its compact film morphology (Fig. S11a† and Fig. S12†). These results reflect that the 3D interpenetrating graphene network increased the rate of charge transfer because of its novel open porous structure and high conductivity. According to the integrated areas of DPV waves, the EASA of 3D-ErGO electrode was measured to be 3.3 times that of 2D-ErGO electrode (Fig. S11b†). The EASA of Ni-Fe/3D-ErGO electrode was calculated to be about 1.64 times that of 3D-ErGO electrode. This is mainly due to that the Ni-Fe LDH nanoplates provided additional EASAs. On the basis of the observations described above, it is reasonable to conclude that the high catalytic performance of Ni-Fe/3D-ErGO electrode for OER is attributed to the synergistic effect of Ni-Fe LDH nanoplates and 3D-ErGO substrate. On the one hand, small sized Ni-Fe LDH nanoplates have more active sites and higher active surface areas, and the turbostratic Ni-Fe LDH structure is benefit for intercalating water molecules and OH^- ions into layered slabs. On the other hand, 3D-ErGO interpenetrating network has higher active surface area than that of a compact ErGO film for loading catalysts, and the superior conductivity of 3D-ErGO enhances the electron transfer between electrolyte ions (OH^-) and electrode. The residual oxygenated functional

groups of ErGO interact with water molecules via hydrogen bonding, increasing the amount of reactants around the electrode. Furthermore, the porous structure of 3D-ErGO provides more accessible surface area for electrolyte and accelerates the release of oxygen gas.[33,40]

The catalytic kinetics of the catalysts has been compared by analyzing the Tafel slopes of OER at different electrodes. The Tafel slope of Ni-Fe/Au, Ni-Fe/2D-ErGO, and Ni-Fe/3D-ErGO electrodes were measured to be 58, 42, and 39 mV dec^{-1}, respectively. These values are much lower than that of Au (112 mV dec^{-1}) or 3D-ErGO (100 mV dec^{-1}) electrode (Fig. S13†, and Table S1†). These results reflect that the OER kinetics is mainly controlled by their Ni-Fe catalysts. The widely accepted mechanism for OER includes four sequential electron transfer steps and each step is coupled with a proton transfer. The intermediates formed in OER process are unstable, and need to be stabilized by active metals. Therefore, the binding strength between active metal sites and intermediates, and the stability of intermediates are the factors that control the kinetics of the rate-determining step.[4] Fig. 3b and Table S1 (ESI †) summarized the overpotentials (at 10 mA cm^{-2}, red curve) and Tafel slopes (black curve) of the above five electrodes. Accordingly, Ni-Fe/3D-ErGO shows the best electrocatalytic performance on both activity and kinetics, and it can be directly used as electrode for OER without blending with binders or other conductive additives.

The performance of Ni-Fe/3D-ErGO electrode depends on the potential used for depositing Ni-Fe LDH nanoplates. The CV curve (Fig. S14†) of 3D-ErGO electrode in Ni-Fe nitrate precursor shows a strong reduction current at the potentials lower than –0.8 V. This current is attributed to the electrochemical reduction of NO_3^- ions to form NH_4^+ and OH^- ions. Simultaneously, Ni^{2+} ions combined with OH^- ions to form insoluble $Ni(OH)_2$ that deposited on the surface of working electrode, and the Fe^{3+} ions in the solution are intercalated into the $Ni(OH)_2$ lattice randomly. Different deposition potentials affect the reduction of ErGO and the growth of Ni-Fe LDH nanoplates, and consequently influence the OER performance of the resulting catalysts. As the deposition potential decreased from –0.8 to –1.2 V, the peaks related to the oxidation of Ni^{2+} ions in the polarization curves of OER increased, indicating the increase in the loading of Ni-Fe LDH nanoplates on the electrode (Fig. 3c). The overpotential and Tafel slope of OER were also tested to be the lowest as the deposition potential was controlled to be –1.2 V (Fig. 3d). Further lowering the deposition potential to –1.3 V, the loading of catalysts was decreased and the catalytic performance was worsened (Fig. 3c, 3d, Fig. S15†, and Table S2†). These results reveal that a proper deposition potential is important for controlling the reduction state of ErGO and the loading of Ni-Fe LDH nanoplates.

The catalytic performance of the Ni-Fe/3D-ErGO electrode also depends on their Ni/Fe atomic ratio (Fig. 3e, 3f, and Fig. S16†, Table S3†).[12,16,19,41,42] The OER overpotential at the electrode prepared from pure Ni or Fe nitrate was tested to be 0.406 and 0.396 V (at 10 mA cm^{-2}, Fig. 3f and Table S3†),

indicating its weak catalytic activity. The doping of Fe in Ni phase significantly decreases the overpotentials of Ni-Fe/3D-ErGO catalysts to be lower than 0.275 V, and a minimum overpotential of 0.259 V was achieved as the Ni/Fe ratio of nitrate precursors was controlled to be 8:2 (4:1). Meanwhile, the current densities of $Ni(OH)_2/NiOOH$ oxidation waves decrease regularly and the potentials related to these waves positively shifted with the increase of Fe-doping. This phenomenon was also observed from the thin-film Ni-Fe oxide catalysts reported by Bell's groups.[16] They acquired the *in-suit* Raman spectra of Ni-Fe films during OER, suggesting that the Fe content changed the local environment of Ni-O band, thus altering the redox properties of Ni and increasing the activities of the co-catalyst.[16] It should be noted here that the catalyst prepared from pure Fe nitrate showed an intrinsic extremely high catalytic kinetics with a low Tafel slope of 40 mV dec^{-1}, while that obtained from Ni nitrate had a poor kinetics with a large Tafel slope of 83 mV dec^{-1} (Fig. 3f, Fig. S16† and Table S3†). When doping Fe in Ni structure, the kinetics of Ni-Fe catalyst is obviously improved compared with pure Ni catalyst. The catalyst prepared by electrodeposition of Ni-Fe LDH nanoplates from the nitrate precursors with Ni/Fe molar ratio of 8:2 (or 4:1) showed the highest kinetics with a small Tafel slope of 39 mV dec^{-1}. This is possibly due to that the doping of Fe^{3+} ions increased the conductivity of the co-catalyst or generates more favorable sites for OER intermediates.[13] On the basis of the observations described above, we conclude that the incorporation of Fe in Ni structure can increase the activity and kinetics of Ni-Fe/3D-ErGO catalysts and the atomic ratio of 8:2 in the precursor solution is a proper ratio for optimizing both overpotential and Tafel slope.

The influence of the loading density of 3D-ErGO on OER performance was also investigated. We nominated the electrodes with different amounts of 3D-ErGO as Ni-Fe/3D-ErGO_t, where t is the time in second used for reducing GO dispersion. With the increase of t, the thickness of the interpenetrating network of Ni-Fe/3D-ErGO increases (Fig. S17a-c †). CV studies of Ni-Fe/3D-ErGO_t electrodes in an aqueous solution of 5 mM $K_4[Fe(CN)_6]$ containing 1 M KCl indicate that both the capacitance and the peak current increased with the increase of t. However, the potential separation of redox waves (ΔE_p) was increased from 37 mV for Ni-Fe/3D-ErGO_5 to 44 mV for Ni-Fe/3D-ErGO_40 (Fig. S17d†), reflecting the slowing down of electron transfer in the electrodes because of the distance elongation of electron transfer. By calculating the integrated areas of DPV waves (Fig. S17e†), the EASAs of Ni-Fe/3D-ErGO_10 and Ni-Fe/3D-ErGO_20 were measured to be 2.6 and 4.5 times that of Ni-Fe/3D-ErGO_5. Thus, at t = 10 s, the EASA of electrode increased most dramatically. The activity of OER was also increased with t because of reducing the overpotential at 10 mA cm^{-2}. The CV wave related to the oxidation reaction of Ni^{2+} to Ni^{3+} slightly right shifted with a little wave deformation simultaneously. This is because that a large amount of 3D-ErGO provided a large capacitive current to alter the behavior of the Ni-Fe catalyst. Accordingly, the Ni-Fe/3D-ErGO_10 has an optimized
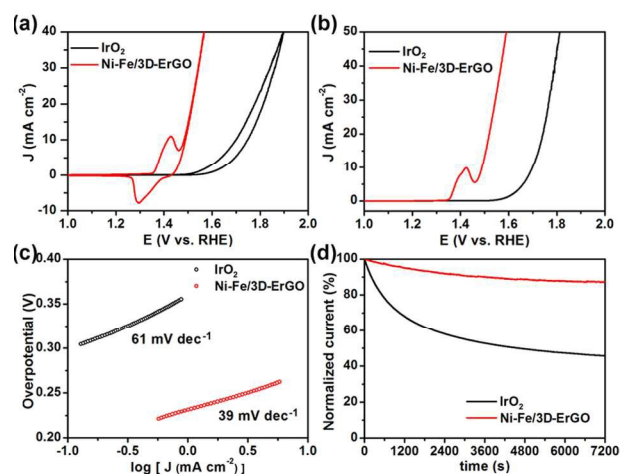
Fig. 4 (a) CVs, (b) LSVs, (c) Tafel plots and (d) Current density – time (j – t) curves of Ni-Fe/3D-ErGO (at 1.490 V) and IrO$_2$ (at 1.70 V) electrodes in the aqueous solution of 1 M KOH.

Fig. 5 Faradaic efficiency measurement for the Ni-Fe/3D-ErGO RRDE in 1 M KOH at a rotating rate of 1600 rpm under N$_2$ atmosphere. The disk and ring currents, and the Faradaic efficiency of RRDE are plotted as functions of the applied disk potential. The ring potential is at a constant potential of 0.32 V (vs. RHE).

porous structure and a promising EASA for the electrochemical catalysis of OER.

3.4 Comparison with IrO$_2$

Noble-metal oxide IrO$_2$ has been widely used as a standard catalyst for OER in alkaline media to evaluate the performance of other catalysts.[1,3] The CV curve of Ni-Fe/3D-ErGO electrode (Fig. 4a) shows a couple of *quasi*-reversible redox waves, relating to the transformation between α-Ni(OH)$_2$ and γ-NiOOH. Furthermore, in the potential range of 1.5 to 1.6 V (vs. RHE), the anodic and cathodic curves are nearly overlapped, indicating the fast recovery of the active sites of this catalyst during OER. In comparison, in the CV curve of IrO$_2$ (Fig. 4a), the current density of cathodic curve is much lower than that of anodic curve at a given potential in the range of 1.5 to 1.9 V, indicating the degradation of the catalyst during OER. The LSV curves (Fig. 4b) and Tafel plots (Fig. 4c) indicate that Ni-Fe/3D-ErGO outperforms IrO$_2$ both in activity and kinetics, exhibiting a lower overpotential of 0.259 V than that of IrO$_2$ (0.470 V) and a smaller Tafel slope of 39 mV dec^{-1} than that of IrO$_2$ (61 mV dec^{-1}). The electrochemical stabilities of Ni-Fe/3D-ErGO and IrO$_2$ were also tested by chronoamperometry (j – t) technique at a constant potential (the potential at which to reach a current density of 10 mA cm^{-2}) (Fig. 4d). The Ni-Fe/3D-ErGO electrode remained about 90% of its initial current density after operation at a constant potential of 1.490 V (vs. RHE) for 2h, while the IrO$_2$ only remained about 50% initial current density at a constant potential of 1.70 V (vs. RHE). It is well-known that IrO$_2$ has a poor long-term stability in alkaline media because of the inevitable aggregation of IrO$_2$ nanoparticles, resulting in the decrease of active sites.[3] Actually, the distributed IrO$_2$ nanoparticles on the pristine electrode became obscure on the surface which was caused by heavily aggregation after the stability test (Fig. S18 †). In a sharp contrast, the morphologies of Ni-Fe/3D-ErGO electrode showed little change before (Fig. 1c-f) and after (Fig. S19†) the

stability test. Thus our Ni-Fe/3D-ErGO electrode exhibited much better tolerance of chemical corrosion than IrO$_2$. This is mainly due to the stable 3D interpenetrating framework of ErGO and the *in-suit* conversion of α-Ni(OH)$_2$ to γ-NiOOH without mechanical deformation or swelling of the structure (Fig. S19c† and Fig. S19d†).[43,44]

3.5 Faradaic efficiency

The Faradaic efficiency of Ni-Fe/3D-ErGO catalyst for OER was measured by RRDE technique and calculated by following equation:[19]

$$\text{Faradaic efficiency} = \frac{n_{app} \times i_r}{i_d \times N}$$

where n$_{app}$ is the apparent number of electrons, and it was reported to be 2 at a rotating rate of 1600 rpm;[6] i$_r$ and i$_d$ are the measured ring and disk currents, respectively, and N is the collection efficiency (0.29 ± 0.01, Fig. S20†).[45] For the system of Ni-Fe/3D-ErGO catalyst in 1 M KOH, the plots of i$_r$, i$_d$, and Faradaic efficiency versus the potential applied to disk electrode are shown in Fig. 5. Accordingly, the Faradaic efficiencies were calculated to be in the range of 93% to around 60 % as the disk potential varied from 1.459 to 1.499 V (vs. RHE). The decreasing of Faradaic efficiency with the increase of potential at disk electrode was caused by the generation of oxygen bubbles; only dissolved oxygen can be reduced at the surface of the Pt ring electrode. Thus, the 93% Faradaic efficiency obtained at 1.459 V (vs. RHE, disk potential) is representative to this OER system. Actually, the current density (about 1 mA cm^{-2}) at this potential is sufficiently large to generate fully dissolved oxygen without forming oxygen bubbles at disk electrode.[6]

4. Conclusions

We developed a two-step electrochemical method for the fabrication of Ni-Fe/3D-ErGO electrode, and it can be directly

used for efficient water oxidation without blending any binders or other conductive additives. This method is simple, time-saving and eco-friendly, avoiding the complicated CVD or hydrothermal process. Particularly, it is readily scalable into industrial levels. This 3D electrode outperforms the precious IrO_2 catalyst modified electrode in activity, kinetics and stability. Its excellent performance is originated from the synergistic effect of the nanosized Ni-Fe LDH nanoplates and the 3D interpenetrating network of graphene. The Ni-Fe/3D-ErGO electrode is promising for the practical application in electrochemical water splitting and the technique developed here can be extended to fabricate the high-performance electrocatalytic electrodes.

Acknowledgements

Notes and references

Department of chemistry, Tsinghua University, Beijing 100084, People's Republic of China.

E-mail: gshi@tsinghua.edu.cn;

Fax: +86-10-62771149;

Tel: +86-10-62773743

1. L. Trotochaud and S. W. Boettcher, *Scripta Mater.*, 2014, **74**, 25.
2. T. R. Cook, D. K. Dogutan, S. Y. Reece, Y. Surendranath, T. S. Teets and D. G. Nocera, *Chem. Rev.*, 2010, **110**, 6474.
3. M. G. Walter, E. L. Warren, J. R. McKone, S. W. Boettcher, Q. Mi, E. A. Santori and N. S. Lewis, *Chem. Rev.*, 2010, **110**, 6446.
4. I. C. Man, H.-Y. Su, F. Calle-Vallejo, H. A. Hansen, J. I. Martinez, N. G. Inoglu, J. Kitchin, T. F. Jaramillo, J. K. Norskov and J. Rossmeisl, *ChemCatChem*, 2011, **3**, 1159.
5. Y. Lee, J. Suntivich, K. J. May, E. E. Perry and Y. Shao-Horn, *J. Phys. Chem. Lett.*, 2012, **3**, 399.
6. C. C. L. McCrory, S. H. Jung, J. C. Peters and T. F. Jaramillo, *J. Am. Chem. Soc.*, 2013, **135**, 16977.
7. J. Suntivich, K. J. May, H. A. Gasteiger, J. B. Goodenough and Y. Shao-Horn, *Science*, 2011, **334**, 1383.
8. A. Grimaud, K. J. May, C. E. Carlton, Y.-L. Lee, M. Risch, W. T. Hong, J. Zhou and Y. Shao-Horn, *Nat. Commun.*, 2013, **4**, 2439.
9. X. X. Zou, J. Su, R. Silva, A. Goswami, B. R. Sathe and T. Asefa, *Chem. Commun.*, 2013, **49**, 7522.
10. L. Trotochaud, J. K. Ranney, K. N. Williams and S. W. Boettcher, *J. Am. Chem. Soc.*, 2012, **134**, 17253.
11. P. W. Du and R. Eisenberg, *Energy Environ. Sci.*, 2012, **5**, 6012.
12. L. Trotochaud, S. L. Young, J. K. Ranney and S. W. Boettcher, *J. Am. Chem. Soc.*, 2014, **136**, 6744.
13. D. A. Corrigan, *J. Electrochem. Soc.*, 1987, **134**, 377.
14. E. L. Miller and R. E. Rocheleau, *J. Electrochem. Soc.*, 1997, **144**, 3072.
15. M. Gong, Y. Li, H. Wang, Y. Liang, J. Z. Wu, J. Zhou, J. Wang, T. Regier, F. Wei and H. Dai, *J. Am. Chem. Soc.*, 2013, **135**, 8452.
16. M. W. Louie and A. T. Bell, *J. Am. Chem. Soc.*, 2013, **135**, 12329.
17. F. Song and X. Hu, *Nat. Commun.*, 2014, **5**, 4477.
18. A. J. Esswein, M. J. McMurdo, P. N. Ross, A. T. Bell and T. D. Tilley, *J. Phys. Chem. C*, 2009, **113**, 15068.
19. Y. Qiu, L. Xin and W. Li, *Langmuir.*, 2014, **30**, 7893.
20. D. Tang, J. Liu, X. Wu, R. Liu, X. Han, Y. Han, H. Huang, Y. Liu and Z. Kang, *ACS Appl. Mater. Interfaces*, 2014, **6**, 7918.
21. X. Long, J. Li, S. Xiao, K. Yan, Z. Wang, H. Chen and S. Yang, *Angew. Chem. Int. Edit.*, 2014, **53**, 7584.
22. B. S. Yeo and A. T. Bell, J. Am. Chem. Soc., 2011, **133**, 5587.
23. M. E. G. Lyons, A. Cakara, P. O'Brien, I. Godwin and R. L. Doyle, *Int. J. Electrochem. Sci.*, 2012, **7**, 11768.
24. S. Guo and S. Sun, *J. Am. Chem. Soc.*, 2012, **134**, 2492.
25. C. Li and G. Shi, *Nanoscale*, 2012, **4**, 5549.
26. S. Chen, J. Duan, J. Ran, M. Jaroniec and S. Z. Qiao, *Energy Environ. Sci.*, 2013, **6**, 3693.
27. J. Wang, H.-x. Zhong, Y.-l. Qin and X.-b. Zhang, *Angew. Chem. Int. Edit.*, 2013, **52**, 5248.
28. W. S. Hummers and R. E. Offeman, *J. Am. Chem. Soc.*, 1958, **80**, 1339.
29. K. Sheng, Y. Sun, C. Li, W. Yuan and G. Shi, *Sci. Rep.*, 2012, **2**, 247.
30. Y. Li, K. Sheng, W. Yuan and G. Shi, *Chem. Commun.*, 2013, **49**, 291.
31. X. Yu, K. Sheng and G. Shi, *Analyst*, 2014, **139**, 4525.
32. Y. Xu, K. Sheng, C. Li and G. Shi, *ACS Nano*, 2010, **4**, 4324.
33. S. Chen, J. Duan, M. Jaroniec and S. Z. Qiao, *Angew. Chem. Int. Edit.*, 2013, **52**, 13567.
34. J. Chen, B. Yao, C. Li and G. Shi, *Carbon*, 2013, **64**, 225.
35. L. Xu, Y.-S. Ding, C.-H. Chen, L. Zhao, C. Rimkus, R. Joesten and S. L. Suib, *Chem. Mater.*, 2008, **20**, 308.
36. G. Soler-Illia, M. Jobbagy, A. E. Regazzoni and M. A. Blesa, *Chem. Mater.*, 1999, **11**, 3140.
37. K. N. Kudin, B. Ozbas, H. C. Schniepp, R. K. Prud'homme, I. A. Aksay and R. Car, *Nano Lett.*, 2008, **8**, 36.
38. H. Wang, J. T. Robinson, X. Li and H. Dai, *J. Am. Chem. Soc.*, 2009, **131**, 9910.
39. S. Wu, Z. Zeng, Q. He, Z. Wang, S. J. Wang, Y. Du, Z. Yin, X. Sun, W. Chen and H. Zhang, *Small*, 2012, **8**, 2264.
40. S. Chen, J. Duan, M. Jaroniec and S.-Z. Qiao, *Adv. Mater.*, 2014, **26**, 2925.
41. Y.-F. Li and A. Selloni, *ACS Catalysis*, 2014, **4**, 1148.
42. L. Kuai, J. Geng, C. Chen, E. Kan, Y. Liu, Q. Wang and B. Geng, *Angew. Chem. Int. Edit.*, 2014, **53**, 7547.
43. M. Gao, W. Sheng, Z. Zhuang, Q. Fang, S. Gu, J. Jiang and Y. Yan, *J. Am. Chem. Soc.*, 2014, **136**, 7077.
44. J. Ran, J. Zhang, J. Yu, M. Jaroniec and S. Z. Qiao, *Chem. Soc. Rev.*, 2014, **43**, 7787.
45. U. A. Paulus, T. J. Schmidt, H. A. Gasteiger and R. J. Behm, *J. Electroanal. Chem.*, 2001, **495**, 134.

Entry of Graphical Abstract
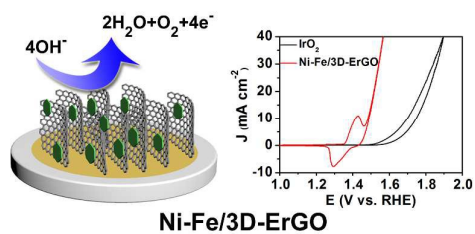
Ni-Fe/3D-ErGO

Ni-Fe layered double hydroxide nanoplates loaded on three-dimensional electrochemically reduced graphene oxide electrode for efficient water oxidation, exhibiting higher activity, kinetics, and stability than those of IrO_2 catalyst.